Cancer Medicine

WILEY

Cancer Medicine Open Access

RESEARCH ARTICLE OPEN ACCESS

Identification of Novel Small-Molecule Inhibitors Targeting KDM5B and Evaluation of Their Antitumour Effects

Tomoaki Hara[1] | Sikun Meng[1] | Masamitsu Konno[1,2] | Naohiro Nishida[3] | Jun Koseki[1,2] | Kanji Meguro[4] | Yasuhiko Kawano[4] | Toshiya Morie[4] | Shingo Dan[5] | Taroh Satoh[3] | Shuji Akai[4] | Kazutake Tsujikawa[4] | Hidetoshi Eguchi[3] | Masaki Mori[6] | Yutaka Miura[7] | Nobuhiro Nishiyama[7] | Hideshi Ishii[1]

[1]Department of Medical Data Science, Center of Medical Innovation and Translational Research, Graduate School of Medicine, The University of Osaka, Suita, Osaka, Japan | [2]Cellular and Molecular Biotechnology Research Institute, National Institute of Advanced Industrial Science and Technology, Tokyo, Japan | [3]Department of Gastroenterological Surgery, Graduate School of Medicine, The University of Osaka, Suita, Osaka, Japan | [4]Graduate School of Pharmaceutical Sciences, The University of Osaka, Suita, Osaka, Japan | [5]Division of Molecular Pharmacology, Cancer Chemotherapy Center, Japanese Foundation for Cancer Research, Tokyo, Japan | [6]Tokai University Graduate School of Medicine, Isehara, Kanagawa, Japan | [7]Department of Life Science and Technology, School of Life Science and Technology, Institute of Science Tokyo, Yokohama, Kanagawa, Japan

Correspondence: Hideshi Ishii (hishii@gesurg.med.osaka-u.ac.jp)

Received: 11 March 2026 | **Revised:** 2 June 2026 | **Accepted:** 12 June 2026

Keywords: histone demethylases | JB-157 | JB-161 | KDM5B | stem cell markers

ABSTRACT

KDM5B, a member of the KDM5 family of histone demethylases, plays a critical role in transcriptional repression by demethylating H3K4me2/3. It regulates key biological processes such as development, stem cell maintenance, and oncogenesis, and its aberrant expression is implicated in various cancers. Accordingly, KDM5B is considered a promising therapeutic target in cancer drug discovery. In this study, we performed a screening to identify novel inhibitors of KDM5B. Through this screening, we identified a common core scaffold associated with KDM5B inhibitory activity, and subsequent optimization of the side-chain structures led to the identification of a series of compounds with IC_{50} values ranging from several nanomolar to several micromolar. Evaluation of growth inhibitory activity using the JFCR39 human cancer cell line panel revealed that the final lead compounds, JB-157 and JB-161, exhibited GI_{50} values in the low micromolar range. In a xenograft model, where the human colorectal cancer cell line HT-29 was implanted into NOD/SCID mice, administration of these compounds resulted in antitumour effects, with JB-161 showing particularly pronounced tumor suppression in a subset of treated animals. Furthermore, combination treatment with in vivo CAR-T cell therapy and JB-161 in C57BL/6J mice was associated with alterations in chromatin accessibility in tumor and immune cell populations. Taken together, these results suggest that JB-161 is a candidate KDM5B inhibitor associated with chromatin accessibility changes and antitumour activity.

1 | Introduction

Epigenetic modifications, including DNA methylation and histone modifications, are essential regulators of gene expression, cellular identity, and organismal development [1, 2]. Among histone modifications, methylation on specific lysine residues on histone H3 plays important roles in both transcriptional activation and repression, depending on the methylation site and degree [3]. Histone H3 lysine 4 trimethylation (H3K4me3) is generally associated with transcriptionally active promoters,

Abbreviations: 5-FU, 5-fluorouracil; ATP, Adenosine Triphosphate; CAF, Cancer-associated fibroblast; CAR, Chimeric antigen receptor; CSC, Cancer stem cell; DMA, N, N-dimethylacetamide; DMF, N, N-dimethylformamide; DMSO, Dimethyl sulfoxide; EMT, Epithelial-to-mesenchymal transition; GSEA, Gene set enrichment analysis; HCC, Hepatocellular carcinoma; HRP, Horseradish peroxidase; IC_{50}, Half-maximal inhibitory concentration; IKK, IκB kinase; IL, Interleukin; IVT, In vitro transcription; JmjC, Jumonji C; KDM, Lysine demethylase; LNP, Lipid nanoparticle; m^6A, N6-methyladenosine; MG-MID, Mean graph midpoint; NOD/SCID, Non-obese diabetic/severe combined immunodeficient; PDAC, Pancreatic ductal adenocarcinoma; RNA-seq, RNA sequencing; rRNA, Ribosomal RNA; scRNA-seq, Single-cell RNA sequencing; TCR, T cell receptor; TGF, Transforming growth factor; TLR, Toll-like receptor; TNBC, Triple-negative breast cancer.

whereas methylation of H3K9 and H3K27 is linked to transcriptional repression [4]. The dynamic regulation of histone methylation is mediated through the coordinated activities of histone methyltransferases and histone demethylases [5, 6]. The discovery of Jumonji C (JmjC) domain-containing histone demethylases demonstrated that histone methylation is a reversible and highly regulated process involved in development, cellular senescence, and disease pathogenesis [7–9]. Among these enzymes, the lysine demethylase 5 (KDM5) family, consisting of KDM5A-D, specifically catalyzes the demethylation of H3K4me2/3 and thereby contributes to transcriptional repression [10]. KDM5 family members have distinct biological functions; for example, KDM5A and KDM5C are implicated in neural development, and KDM5C mutations are associated with X-linked intellectual disability [11, 12]. KDM5B (also known as PLU-1 or JARID1B) has been reported to regulate embryonic development, stem cell maintenance, and lineage specification [13, 14]. Importantly, aberrant KDM5B expression has been observed in multiple malignancies, including breast, prostate, and lung cancers, where it contributes to tumor progression through repression of tumor suppressor genes, promotion of epithelial–mesenchymal transition, maintenance of cancer stem-like properties, and induction of therapeutic resistance [15–17].

Given its oncogenic functions, KDM5B has emerged as a promising therapeutic target. Early KDM5 inhibitors, such as CPI-455, demonstrated that pharmacological inhibition of KDM5 increases global H3K4me3 levels and enhances the effects of DNA demethylating agents, including 5-aza-2′-deoxycytidine, in cancer cells [18]. Subsequent studies identified additional inhibitors, including KDM5-Inh1 and KDOAM-25, which exhibited selective inhibition of KDM5 demethylases and suppressed tumor cell growth in models of multiple myeloma and HER2-positive breast cancer [19, 20]. However, the clinical development of KDM5 inhibitors remains challenging because many currently available compounds exhibit limited selectivity, insufficient in vivo potency, suboptimal pharmacokinetic properties, and potential off-target effects [21, 22].

Therefore, there is an ongoing need to develop potent KDM5-targeting inhibitors with improved selectivity and favorable drug-like properties. In the present study, we conducted a comprehensive screening, coupled with biochemical and cellular assays, to identify and characterize novel KDM5B inhibitors with antitumour effect in vitro and in vivo. These findings provide a basis for the development of next-generation epigenetic therapies targeting KDM5B-driven cancers.

2 | Materials and Methods

2.1 | Compound Library and Screening

The in vitro screening was conducted at the Center for Supporting Drug Discovery and Life Science Research, the University of Osaka, using a compound library owned by the same institution. For in silico screening, a compound library provided by Namiki Shoji Co. Ltd. (Tokyo, Japan) was used, and molecular docking was performed using the Glide docking program in Schrödinger Suite 2014 (Schrödinger LLC, New York, NY, USA).

2.2 | Synthesis of KDM5B Inhibitors

Each compound was synthesized according to the synthetic scheme shown in Figure S2.

For the synthesis of JB-157, a suspension of 1 mmol of 5-amino-1-[3-(trifluoromethoxy)phenyl]-3-methyl-1H-pyrazole-4-carboxamide in 1.5 mL of isopropanol was prepared, followed by the addition of 3 mmol of ethyl difluoroacetate and 1.2 mL of a 5 M sodium methoxide methanol solution. The mixture was refluxed in an oil bath for 2 h. After cooling to room temperature, 10 mL of ice water was added, and the pH was adjusted to 3.0 with 6 N hydrochloric acid under stirring. The resulting precipitate was collected by filtration, washed with water, and dried to give 6-difluoromethyl-1,5-dihydro-1-[3-(trifluoromethoxy)phenyl]-3-methyl-4H-pyrazolo[3,4-d]pyrimidin-4-one. A suspension of 0.83 mmol of this compound in 10 mL of toluene was treated with 0.83 mmol of Lawesson's reagent and refluxed in an oil bath for 2.5 h. After cooling to room temperature, 10 mL of ice water and 2 mL of 2 N sodium hydroxide solution were added, and the mixture was extracted. The aqueous layer was washed with toluene, adjusted to pH 3.0 with 6 N hydrochloric acid, and the precipitate was collected by filtration, washed with water, and dried. The obtained solid was washed with n-hexane/ethyl acetate (10:1) to afford 6-difluoromethyl-1,5-dihydro-1-[3-(trifluoromethoxy)phenyl]-3-methyl-4H-pyrazolo[3,4-d]pyrimidine-4-thione (JB-157).

^{1}H NMR (DMSO-d_6) δ: 2.53 (3H, s), 6.81 (1H, t, J = 53.0 Hz), 7.36 (1H, d, J = 8.0 Hz), 7.67 (1H, t, J = 8.0 Hz), 8.09 (1H, s), 8.12 (1H, d, J = 8.0 Hz), 13.3 (1H, br s). For the synthesis of JB-161, the same procedure used for JB-157 was followed. 5-amino-1-[3-(trifluoromethylsulfanyl)phenyl]-3-methyl-1H-pyrazole-4-carboxamide was reacted with ethyl trifluoroacetate under the same conditions to afford 1,5-dihydro-3-methyl-6-trifluoromethyl-1-[3-(trifluoromethylsulfanyl)phenyl]-4H-pyrazolo[3,4-d]pyrimidine-4-thione (JB-161).

^{1}H NMR (DMSO-d_6) δ: 2.71 (3H, s), 7.71–7.74 (2H, m), 8.20 (1H, m), 8.36 (1H, s). Other derivatives were synthesized in a similar manner using appropriately substituted analogs. The synthesis of compound 1 in Figure S2 was performed according to a previously reported procedure [23, 24]. The corresponding carbonitrile derivative (approximately 4 mmol) was added to concentrated sulfuric acid and stirred in an ice bath for 15 min, then warmed to room temperature and stirred for an additional 1 h. The reaction mixture was poured into ice water, and the pH was adjusted to 4.0 with 2 N sodium hydroxide solution. The resulting precipitate was washed with water and dried.

2.3 | Measurement of Enzyme Inhibition

The JARID1B (KDM5B) Chemiluminescent Assay Kit (BPS Bioscience) was used to evaluate the enzymatic inhibition. The assay begins with a one-hour incubation of the KDM enzyme with a methylated H3 peptide substrate in the presence of KDM5B inhibitors. Subsequently, a primary antibody specific to the demethylated product is added. This is followed by the addition of an HRP-conjugated secondary antibody and a chemiluminescent substrate. The resulting signal is then detected using

a chemiluminescence plate reader. A total of 200 ng of KDM5B was used in a 50 μL reaction volume, and KDM5B inhibitors were added at concentrations ranging from nM to μM. Data represent the mean of two independent experiments ($n = 2$).

2.4 | Measurement of Sphere Formation Inhibitory Activity

MCF-7 cells were routinely maintained in DMEM supplemented with 10% FBS and 1% penicillin/streptomycin under standard culture conditions at 37°C in a humidified incubator with 5% CO_2. For sphere formation assays, cells were seeded at a density of 4000 cells per well in 96-well Ultra-Low Attachment Microplates (Corning) to prevent cell adhesion and promote spheroid formation. The cells were cultured in serum-free DMEM/F12 medium containing 20 ng/mL EGF, 10 ng/mL FGF, 2% MACS NeuroBrew-21 (Miltenyi Biotec), and 1% penicillin/streptomycin. KDM5B inhibitors were dissolved in DMSO and added to the culture medium at concentrations ranging from nM to μM. The final DMSO concentration was adjusted to the same level across all experimental conditions, including vehicle controls and compound-treated samples, and was maintained at 0.5%. After 4 days of incubation, the number of spheres with a diameter greater than 100 μm in each well was counted and compared with that of the control group treated with DMSO alone. Data represent the mean of two independent experiments ($n = 2$).

2.5 | Cell Viability Assay and JFCR39 Analysis

The growth-inhibitory activity and potential KDM5B inhibitors were evaluated using the JFCR39 drug discovery system [25]. The JFCR39 panel comprises 39 human cancer cell lines cultured in 96-well plates. Cells were treated with KDM5B inhibitors for 48 h, after which cell viability was assessed using the sulforhodamine B (SRB) assay. The concentration of KDM5B inhibitors required to inhibit cell growth by 50% (GI_{50}) was determined from the dose–response curves. A fingerprint plot was generated by calculating the deviation of the log GI_{50} of each cell line from the mean log GI_{50} across the panel (MG-MID), which represents the average sensitivity of the 39 cell lines to the compound. Compounds were tested using serial dilutions over a concentration range appropriate for each compound, typically spanning submicromolar to high micromolar concentrations. Each condition was evaluated in at least triplicate. GI_{50} values were determined by nonlinear regression fitting of the dose–response curves using the JFCR39 analytical pipeline based on SRB assay measurements obtained after 48 h of treatment. JB-157 and JB-161 were evaluated over a concentration range of 1 μM to 100 μM using serial dilution conditions in the JFCR39 human cancer cell line panel.

2.6 | Synthesis of mRNA and Lipid Nanoparticles (LNPs)

Plasmids encoding the *FAPCAR* gene (GenScript Biotech Corp.) were transformed into *E. coli* (Thermo Fisher Scientific, Cat# C404010) for propagation. Plasmid DNA was extracted using the Plasmid Midi Kit (QIAGEN, Cat# 12145), followed by linearization with *Hind* III restriction enzyme (Nippon Gene Co. Ltd., Cat# 311–01163). The linearized DNA was then purified by ethanol precipitation. In vitro transcription was performed using the IVTpro T7 mRNA Synthesis System (Takara Bio Inc., Cat# 6144), supplemented with CleanCap Reagent AG (TriLink, Cat# N-7113) and N1-Methylpseudouridine-5′-Triphosphate (TriLink, Cat# N-1081) to generate capped and modified *FAPCAR* mRNA. Each dose for downstream applications contained 10 μg of mRNA. mRNA encapsulation into lipid nanoparticles (LNPs) was conducted using the Lipid Nanoparticle (LNP-0315) Exploration Kit (Cayman Chemical, Cat# 36426) following the manufacturer's protocol. For mRNA containing N6-methyladenosine (m6A) modifications, Adenosine Triphosphate (ATP) in the transcription reaction was substituted with N6-Methyladenosine-5′-Triphosphate (TriLink, Cat# N-1013).

2.7 | Ethics and Animal Experimental Procedures

All animal procedures were approved by the Osaka University Animal Experiment Committee (Approval No. 30–011-053) and conducted in accordance with institutional guidelines. All cages and bedding were sterilized by autoclaving prior to use. Gamma-irradiated sterile chow was used for feeding. Eight-week-old wild-type female NOD/SCID mice and C57BL/6J mice (Japan SLC Inc.) were housed in groups of five per cage under controlled conditions (23°C, 12-h light/dark cycle). Mice were randomly allocated to each treatment group. For the xenograft model shown in Figure 4, HT-29 human colorectal cancer cells were subcutaneously implanted into the dorsal flank of NOD/SCID mice. On days 4 and 7 post-implantation, mice received intraperitoneal injections of either JB-157 or JB-161 at a dose of 6.69 mg/kg body weight or 5-fluorouracil (5-FU) at 100 mg/kg body weight in a volume of 0.2 mL. Tumors were excised 6 days after the initial treatment. HT-29 human colorectal cancer cells were selected for xenograft experiments because they exhibit stable tumor formation in immunodeficient mice, express KDM5B, and show measurable sensitivity to the identified KDM5B inhibitors in preliminary in vitro analyses. In addition, HT-29 cells provide a relatively stringent model for evaluating in vivo antitumour efficacy of epigenetic inhibitors. For the syngeneic model shown in Figure 5, a mixture of MC38 murine colon carcinoma cells and FAP-expressing NIH/3T3 fibroblasts was subcutaneously implanted into the dorsal flank of C57BL/6J mice. Mice were treated on days 1 and 4 post-implantation with various agents, including 5-FU, anti-PD-1 antibody, anti-CTLA-4 antibody, lipid nanoparticle (LNP)-formulated mRNA, CPI-455, or JB-161, according to the assigned experimental group. Tumors were harvested onward for analysis. HT-29 cells were implanted subcutaneously into the backs of NOD/SCID mice. Treatments were administered by intraperitoneal injection on days 4 and 7 after HT-29 cell transplantation. In the C57BL/6J syngeneic model, MC38 and FAP-expressing 3T3 cells were subcutaneously implanted into the dorsal region of C57BL/6J mice, followed by intravenous administration of 5-FU, anti–PD-1 antibody, anti–CTLA-4 antibody, mRNA-LNP, CPI-455, or JB-161 according to the assigned treatment groups. Antibodies were administered according to standard schedules used in murine immune

checkpoint blockade studies. JB-161 and CPI-455 were dissolved in DMSO and diluted in an appropriate vehicle solution prior to administration. Administration was performed by intravenous injection on days 1, 4, 6, and 8 after tumor implantation unless otherwise indicated.

2.8 | Bulk RNA Sequencing (RNA-Seq)

For the RNA-seq analyses shown in Figure 4, tumor tissues were collected from HT-29 xenograft-bearing NOD/SCID mice treated with DMSO, 5-FU, JB-157, JB-161, JB-157 plus 5-FU, or JB-161 plus 5-FU. Tumors were harvested on day 12 after tumor implantation. For the RNA-seq analyses shown in Figure 5, tumor tissues were collected from the MC38/FAP syngeneic tumor model established in C57BL/6J mice treated with combinations of 5-FU, anti–PD-1 antibody, anti–CTLA-4 antibody, mRNA-LNP, CPI-455, or JB-161, according to the assigned treatment groups. Tumors were collected at the experimental endpoint for transcriptomic analysis. Tumor tissue samples were homogenized in 1 mL of ISOGEN reagent (NIPPON GENE) using a tissue homogenizer. Subsequently, 0.2 mL of chloroform was added, and the mixture was centrifuged to separate the aqueous and organic phases. Total RNA was isolated from the aqueous phase by precipitation with isopropanol. Total RNA extracted from tumors shown in Figure 4 and Figure 5 were submitted to the genome analysis core facility at the Research Institute for Microbial Diseases, the University of Osaka. Ribosomal RNA was depleted using the Ribo-Zero Plus rRNA Depletion Kit (Illumina). mRNA libraries were prepared using the TruSeq Stranded mRNA Sample Preparation Kit (Illumina) for Figure 4 and the SMARTer Stranded Total RNA-Seq Kit v2—Pico Input Mammalian (Takara Bio) for Figure 5. The SMARTer Stranded Total RNA-Seq Kit v2—Pico Input Mammalian was selected for the Figure 5 samples because the tumor tissues obtained after combination immunotherapy frequently yielded relatively limited RNA quantities and contained heterogeneous immune cell populations. Sequencing was performed on the NovaSeq X Plus platform in 151-bp single-end mode for Figure 4 and on the NovaSeq 6000 platform in 101-bp paired-end mode for Figure 5. Sequence reads were quality-filtered and adapter-trimmed using Trimmomatic (v0.39). Reads were aligned to the human reference genome GRCh38 or the mouse reference genome GRCm39 using HISAT2 (v2.2.1) with default parameters. Gene annotation files were obtained from GENCODE. Gene-level read counts were generated using featureCounts (Subread v2.0.3). Differential gene expression analysis was performed using DESeq2 (v1.38.3) in R. Genes with an adjusted p-value (false discovery rate, FDR) < 0.05 were considered significantly differentially expressed unless otherwise stated. Gene set enrichment analysis and pathway analysis were performed using clusterProfiler (v4.6.2), based on the count data obtained (S1 and S2). Normalization was performed independently within each dataset prior to downstream analyses. Pathway enrichment analyses were conducted using normalized count matrices generated by DESeq2. Visualization analyses, including heatmaps and volcano plots, were generated using internally normalized datasets. The heatmap of the top 2000 differentially expressed genes was generated using iDEP 2.01. The RNA-seq datasets corresponding to Figure 4 and Figure 5 were generated and analyzed as independent experiments. Because the biological objectives and sample characteristics differed between the xenograft and syngeneic models, different library preparation kits, sequencing platforms, and read configurations were used. Differential expression and downstream pathway analyses were performed independently within each dataset, and no direct cross-comparison or merged analysis between the two sequencing datasets was conducted.

2.9 | Western Blotting

HT29 cells were seeded in 15-cm dishes and cultured in DMEM supplemented with 10% FBS. JB-157 or JB-161 (100 μg in 30 μL) was added to the culture medium, while control cells received 30 μL of DMSO. HT-29 cells were treated with JB-157 or JB-161 at a final concentration of about 14 μM in culture medium containing 0.15% DMSO. Vehicle control cells received an equivalent final concentration of DMSO without compound treatment. Cells were incubated overnight at 37°C prior to histone extraction. After overnight incubation at 37°C, cells were harvested, and histones were extracted from 1×10^7 cells using the EpiQuik Total Histone Extraction Kit (EpigenTek) according to the manufacturer's instructions. A portion of the extracted histone solution was subjected to SDS–PAGE using Bio-Rad Mini-PROTEAN TGX 4%–15% gels, followed by transfer to a PVDF membrane using the iBlot2 system (Thermo Fisher Scientific) with iBlot2 Transfer Stacks PVDF mini. Protein Ladder One Plus Triple-color for SDS-PAGE (Nacalai Tesque) was used as the molecular weight marker. Membranes were blocked with Blocking One (Nacalai Tesque) in TBST and washed with TBST, then incubated overnight at room temperature with one of the following primary antibodies to evaluate the methylation status of histone H3K4: Mono-Methyl-Histone H3 (Lys4) (D1A9) Rabbit mAb, Di-Methyl-Histone H3 (Lys4) (G64G9) Rabbit mAb, or Tri-Methyl-Histone H3 (Lys4) (C42D8) Rabbit mAb (all from Cell Signaling Technology). After washing with TBST, membranes were incubated with Alexa Fluor 594–conjugated goat anti-rabbit IgG (Life Technologies) as the secondary antibody for 3 h at room temperature. Following additional washes with TBST, fluorescent signals were detected using a ChemiDoc imaging system (Bio-Rad).

2.10 | Chromatin Immunoprecipitation Sequencing (ChIP-Seq)

HT-29 cells cultured under the same conditions as those used for Western blotting were processed using the EpiQuik Chromatin Immunoprecipitation Kit (EpigenTek) according to the manufacturer's instructions. The resulting chromatin solution was incubated with Histone H3 (D1H2) Rabbit mAb (Cell Signaling Technology) pre-bound to Dynabeads Protein G (Invitrogen), and immunoprecipitated DNA was recovered following the kit protocol. The purified DNA was subjected to next-generation sequencing using a NovaSeq X Plus system in 151-bp paired-end mode through the genome analysis core facility at the Research Institute for Microbial Diseases, the University of Osaka. ChIP-seq peaks were identified using MACS2.

2.11 | Single-Cell Assay for Transposase-Accessible Chromatin With Sequencing (scATAC-Seq)

Tumor tissue used for scATAC-seq analysis refers to subcutaneous tumors derived from the syngeneic mouse model described in Figure 5. Specifically, MC38 murine colon carcinoma cells were co-implanted with FAP-expressing NIH/3T3 fibroblasts into C57BL/6J mice, followed by treatment with the indicated therapeutic regimens. scATAC-seq analysis was performed using tumor tissues collected from the FPCR group (mRNA-LNP–induced CAR-T therapy) and the FPCRJ161 group (mRNA-LNP plus JB-161), as indicated by the dotted lines in Figure 5B. One tumor sample per condition was analyzed. Harvested tumor tissues were minced in DMEM containing 10% FBS, ulinastatin, and sivelestat on ice, followed by enzymatic digestion with collagenase D and DNase I at 37°C for 1 h with gentle agitation. The digested samples were filtered through 40 μm strainers, centrifuged, and treated with ACK lysis buffer to remove erythrocytes. Cells were then washed with PBS and collected by centrifugation. Cell nuclei were isolated using the EpiQuik Total Histone Extraction Kit (EpigenTek) according to the manufacturer's instructions and submitted to the genome analysis core facility at the Research Institute for Microbial Diseases, the University of Osaka, for next-generation sequencing. Cell Ranger output files were analyzed using Seurat in R to identify cell clusters. Peak analysis and transcription factor activity were subsequently assessed using Signac in R. The code is provided as Code S1.

2.12 | Statistics

For the enzyme activity inhibition assays, cell proliferation assays, and sphere formation assays shown in Figures 1 and 2, experiments were performed twice ($n = 2$), and IC_{50} values were calculated. For the JFCR39 analysis shown in Figure 3, experiments were performed three times ($n = 3$), and Log GI_{50} values were calculated. Pearson's correlation coefficients were calculated using the −Log GI_{50} values obtained from the JFCR39 panel across all evaluated cell lines. Correlation analysis was performed by comparing the sensitivity profiles of each JB compound with those of reference anticancer agents included in the JFCR39 database using standard statistical methods implemented in R. No arbitrary threshold cutoff was applied during the calculation process itself; compounds exhibiting relatively high correlation coefficients were subsequently selected for visualization and discussion in Figure 3D. For the in vivo experiments shown in Figure 4, each treatment group consisted of five mice ($n = 5$ per group). Comparisons between two groups were performed using unpaired, two-tailed Student's *t*-tests. For multi-group comparisons where applicable, appropriate parametric statistical tests were used as described in the corresponding methods sections. For high-throughput sequencing analyses, differential gene expression analysis was performed using DESeq2 with default model assumptions. Pathway enrichment analyses were conducted using clusterProfiler. Multiple comparisons were handled where appropriate in RNA-seq and enrichment analyses. Statistical significance was defined as $p < 0.05$ (two-sided), unless otherwise specified in the corresponding figure legends. Exact *p*-values are reported when available, and significance levels are indicated using standardized notation. Most statistical analyses and graph generation were performed using Microsoft Excel (version 2604) and R (version 4.3.0 or later), depending on the dataset. Bioinformatics analyses were conducted using established R packages, including DESeq2, clusterProfiler, Seurat, and Signac, together with standard bioinformatics tools as described in the Methods section.

3 | Results

3.1 | KDM5B Is Expressed in Various Types of Cancer Cells

KDM5B expression has been reported across multiple cancer types according to public datasets, including the Human Protein Atlas, and was also detected in our previously established single-cell atlas of pancreatic cancer [26] (Figure S1A). Among cancer cells, KDM5B expression was detected across all clusters, with relatively elevated expression observed in a subset of cells within cluster 3 (Figure S1B). Kaplan–Meier plotter analysis showed that high KDM5B expression was associated with poorer prognosis in both pancreatic and gastric cancer patients (Figure S1C). These findings suggest that KDM5B functions within cells in the tumor microenvironment and that its high expression contributes to cancer malignancy.

3.2 | The Five Identified Compounds Inhibit KDM5B and Suppress Cancer Cell Proliferation

To identify novel inhibitors targeting KDM5B, we conducted both an in silico screening using compound databases and a high-throughput screening from a compound library. In the in silico screening, 5,054,941 compounds were narrowed down to 3068 based on predicted binding affinity to the catalytic domain. Taking into account protein thermal fluctuation and dehydration effects, we further narrowed the list to 475 compounds, and finally to 18 compounds using structural clustering based on scaffold similarity. From a library of 52,720 compounds, we identified 1180 compounds with > 90% inhibition activity via high-throughput in vitro screening. Considering inhibitory potency and compound selectivity observed during screening, 49 compounds were selected for further evaluation. A total of 67 compounds (18 from in silico and 49 from high-throughput screening) were tested in cell-based assays, ultimately yielding five promising compounds (Figure 1A). To assess the inhibitory activity of the five compounds, we first measured their enzymatic IC_{50} values, revealing that among the five compounds, OU-J-19 exhibited the lowest IC_{50} value (2.3 μM), indicating relatively stronger inhibitory activity compared with the other compounds (Figure 1B). We then assessed the anti-proliferative effects of these KDM5B inhibitors on cancer cell lines: Panc-1 (pancreatic cancer), HCT116 (colorectal cancer), and MCF7 (breast cancer). In Panc-1 cells, OU-J-41 exhibited the strongest effect, showing inhibition at concentrations as low as 0.2 μM. OU-J-23 exhibited a gradual dose-dependent inhibitory effect beginning at low concentrations, whereas OU-J-31 showed moderate inhibition that became more apparent around 1 μM. In contrast, OU-J-19 and OU-J-25 exhibited sigmoidal inhibition patterns with sharp effects above ~10 μM (Figure 1C). In HCT116 cells, OU-J-41 again showed the strongest inhibition, completely

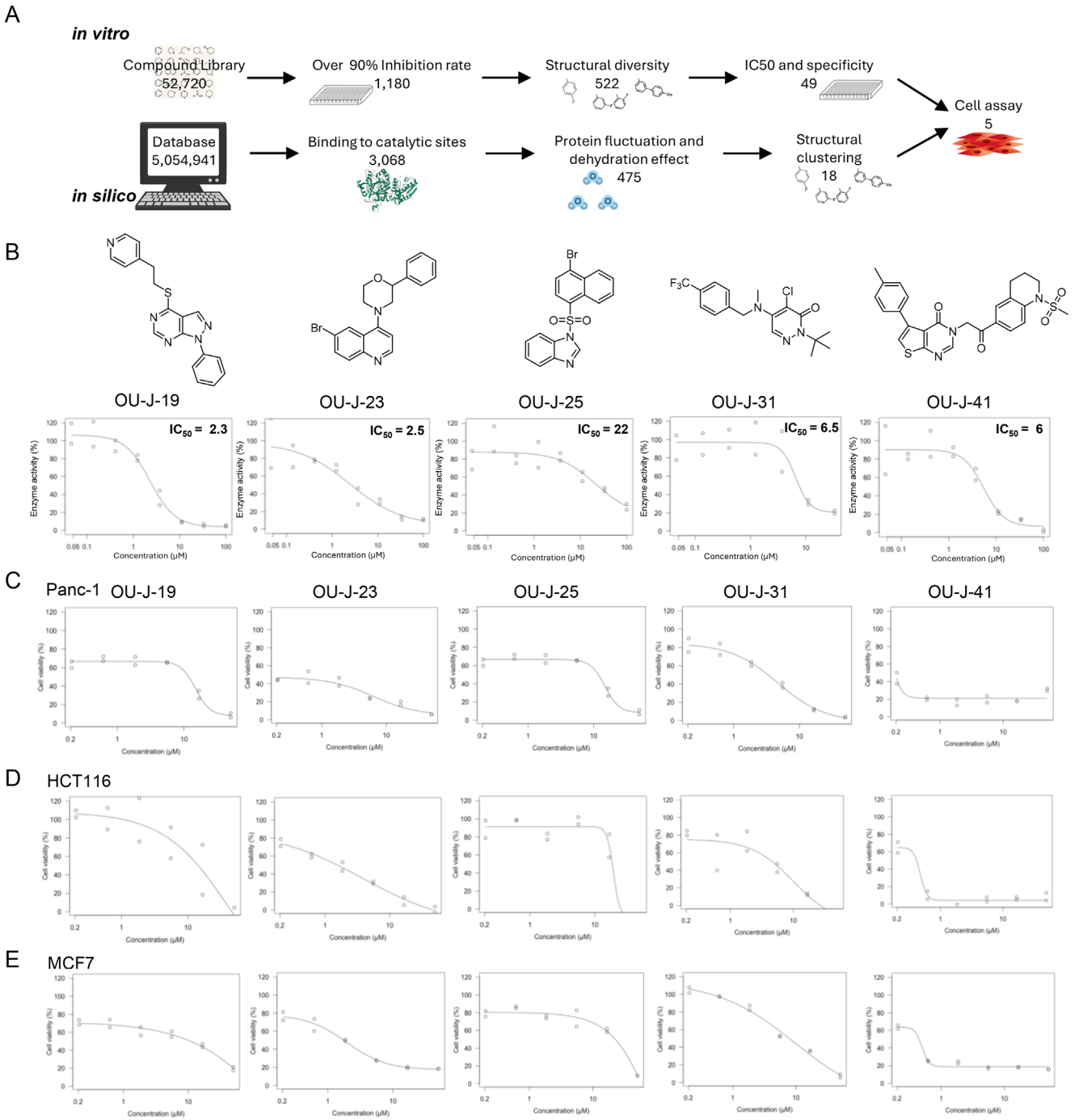

FIGURE 1 | The five identified compounds inhibit KDM5B and suppress cancer cell proliferation. (A) Overview of the screening process. (B) KDM5B enzymatic inhibition assays for the five compounds identified through screening. The IC_{50} values (μM) indicated in the figure represent inhibitory activity, with lower IC_{50} values indicating stronger inhibitory effects. (C) Growth inhibition assay in Panc-1 cells. (D) Growth inhibition assay in HCT116 cells. (E) Growth inhibition assay in MCF7 cells.

suppressing growth at 1 μM. OU-J-23 showed gradual inhibition starting at ~0.2 μM. OU-J-19 and OU-J-31 exhibited similar trends from ~1 μM, and OU-J-25 showed sharp inhibition above ~10 μM (Figure 1D). In MCF7 cells, OU-J-41 was again the most potent, suppressing growth to ~20% at 1 μM. OU-J-31 showed moderate inhibition from ~0.2 μM, while OU-J-19 and OU-J-23 began to inhibit at ~1 μM. OU-J-25 showed strong inhibition only above ~10 μM (Figure 1E). These results confirmed that all five compounds had growth-inhibitory effects on cancer cells.

3.3 | Identification of Essential Modifications for Inhibitory Activity Based on the Common Chemical Structure

To further enhance the inhibitory activity, we attempted synthetic elaboration based on the identified common chemical structure. The core structure was synthesized in six steps using compound 1 and compound 3 as starting materials (Figure S2). This core structure consists of a bicyclic system containing nitrogen atoms—a

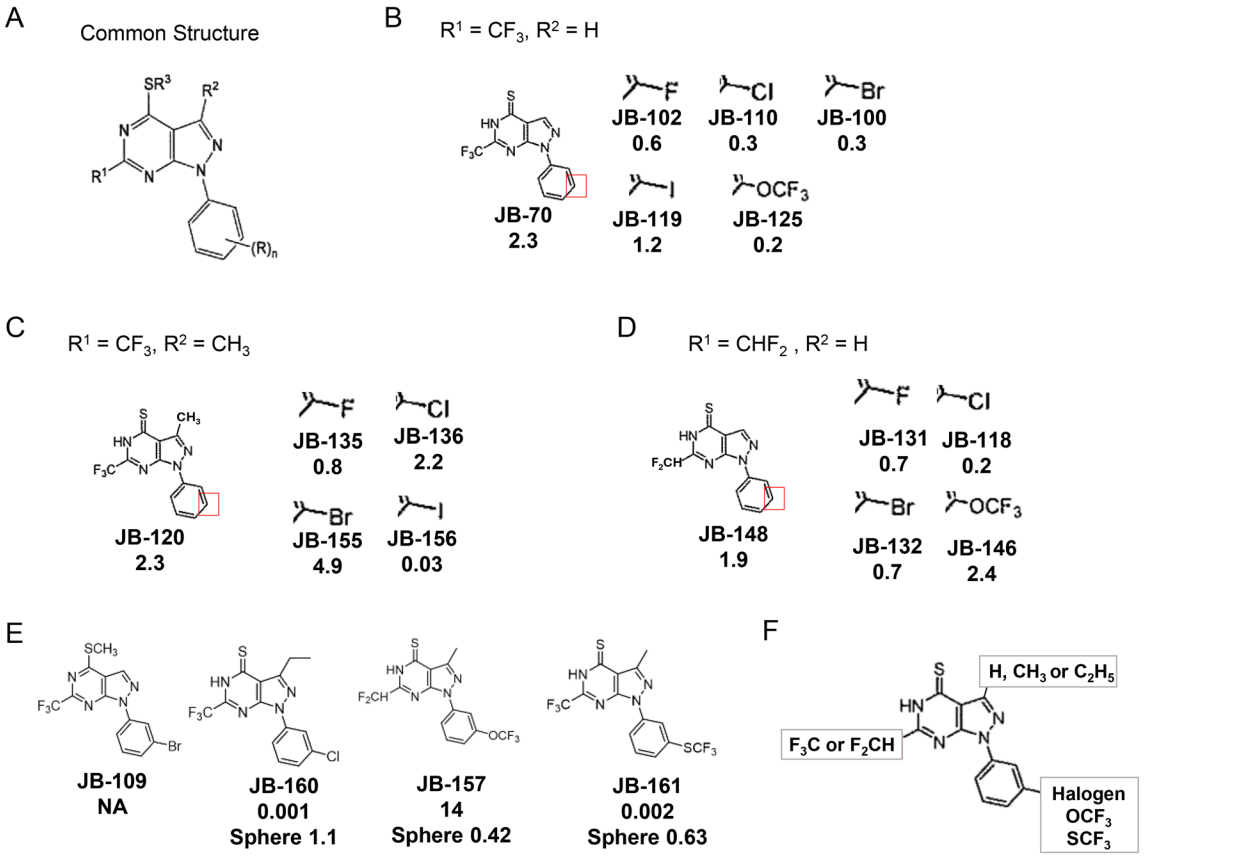

FIGURE 2 | Modifications to the common scaffold affect KDM5B inhibitory activity. (A) Common scaffold of compounds showing KDM5B inhibitory activity. (B) Compounds in which R^1 is CF_3 and R^2 is H. Values indicate IC_{50} (μM). (C) Compounds in which R^1 is CF_3 and R^2 is CH_3. Values indicate IC_{50} (μM). (D) Compounds in which R^1 is CHF_2 and R^2 is H. Values indicate IC_{50} (μM). (E) Other derivative compounds. Values indicate IC_{50} (μM). The "sphere" values in the figure represent the IC_{50} values (μM) obtained from the sphere-forming inhibition assay. (F) Optimized structure of the KDM5B inhibitor. The IC_{50} value was determined through in vitro enzyme inhibition assays.

six-membered and a five-membered heterocycle—with a benzene ring attached to the nitrogen atom of the five-membered ring (Figure 2A). We therefore investigated structural modifications of this common scaffold. JB-70, which has a trifluoromethyl group at R^1 and a hydrogen atom at R^2, exhibited an IC_{50} value of 2.3 μM. In contrast, the introduction of halogen substituents (fluoro, chloro, bromo, or iodo) or a trifluoromethoxy group at the meta-position of the benzene ring further decreased the IC_{50} value (Figure 2B). Similarly, JB-120, with a trifluoromethyl group at R^1 and a methyl group at R^2, showed an IC_{50} of 2.3 μM, while the substitution of the benzene ring at the meta-position with a fluoro or iodo group resulted in a further decrease in IC_{50} (Figure 2C). JB-148, with a difluoromethyl group at R^1 and hydrogen at R^2, had an IC_{50} of 1.9 μM, and the introduction of fluoro, chloro, or bromo groups at the meta-position of the benzene ring further reduced the IC_{50} (Figure 2D). Among these derivatives, several compounds, including JB-157, JB-160, and JB-161, exhibited strong inhibitory profiles in the enzymatic and sphere formation assays, and JB-161 was selected for further investigation based on its overall biological activity profile (Figure 2E). These results suggest that certain fluorinated hydrocarbon groups within the bicyclic core, together with specific halogenated or fluorinated substitutions on the benzene ring, may contribute to enhanced KDM5B inhibitory activity in several derivatives (Figure 2F).

3.4 | The Novel KDM5B Inhibitors Exhibit Antitumour Effects in JFCR39 Cell Panel

We assessed drug sensitivity using a cell proliferation assay in the human cancer cell line panel JFCR39 to evaluate 11 newly synthesized candidate compounds based on the identified core scaffold. JB-157 and JB-161 exhibited growth-inhibitory activity across the panel at concentrations ranging from 1 μM to 100 μM (Figure S3 Figure 3A). Compounds JB-161, JB-160, JB-157, and JB-136 showed higher average-Log GI_{50} values (Average), while JB-146, JB-135, JB-132, and JB-157 exhibited greater variability (Range), as reflected by a wider range between the most and least sensitive cell lines (Figure 3B,C). Comparison with known antitumour agents revealed relatively high similarity in growth inhibition profiles, including positive correlations with several reported KDM5B inhibitors (Figure 3D and Table S1). Since KDM5B expression was confirmed in many cell lines of the JFCR39 panel (Table S2), these eleven JB compounds may represent potential anticancer candidates associated with KDM5B inhibitory activity and cancer cell growth suppression. However, further studies will be required to determine the extent to which the observed antiproliferative effects are directly dependent on KDM5B inhibition in individual cell lines.

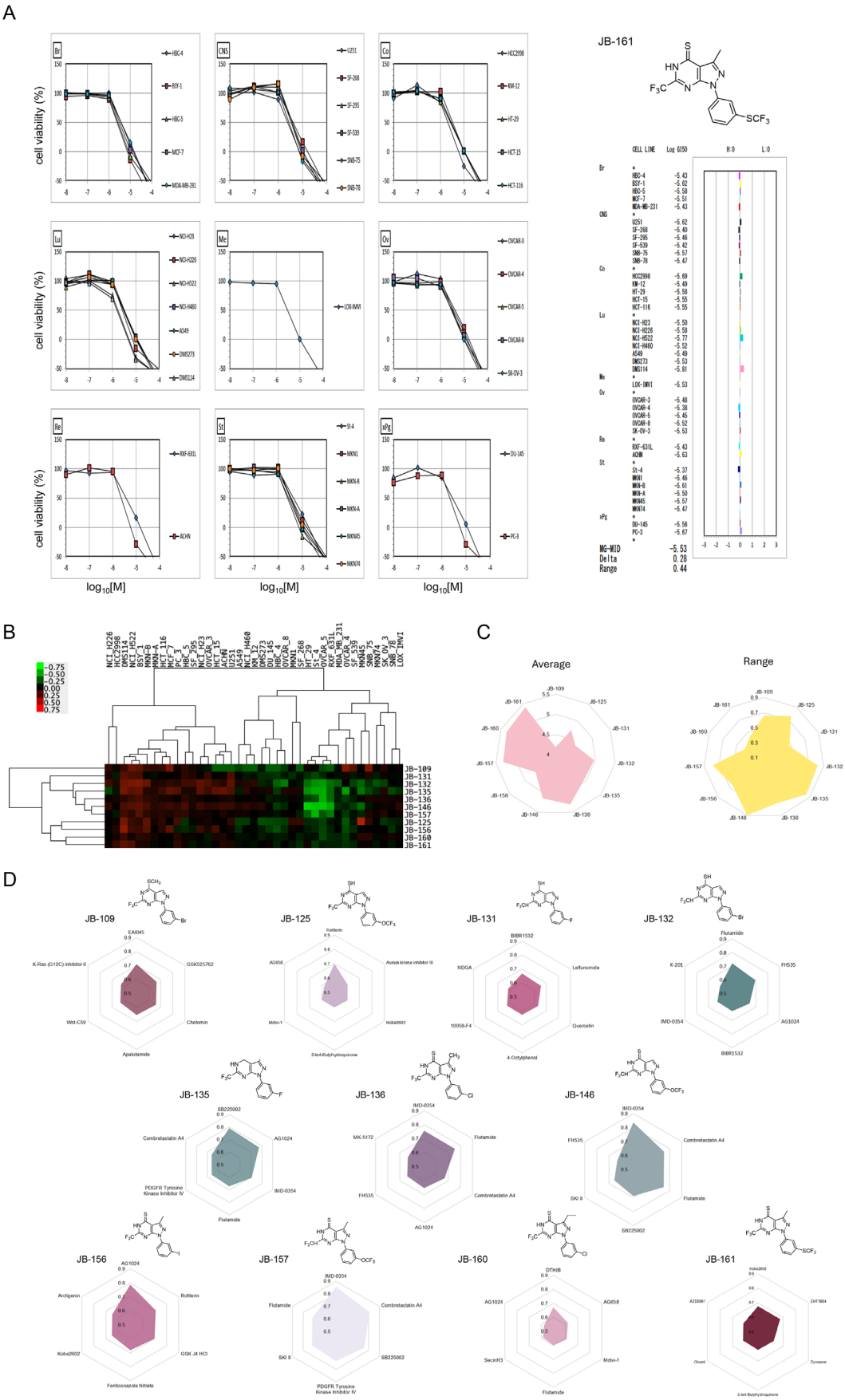

FIGURE 3 | Legend on next page.

FIGURE 3 | Evaluation of compounds using the JFCR39 human cancer cell panel. (A) Cell proliferation assay results using KDM5B inhibitor JB-161. X-axis: Log_{10} drug concentration (M). Y-axis: Relative cell growth (%), normalized to untreated controls (100%). Negative values indicate cytotoxic effects. H and L indicate the numbers of compounds showing high and low correlation, respectively, with the fingerprint pattern of the tested compound in the COMPARE analysis based on Log GI_{50} values across the JFCR39 panel. H:0 and L:0 indicate that no compounds with high or low correlation were identified. (B) Heatmap showing the growth-inhibitory effects of each KDM5B inhibitor across different cell lines. Higher values indicate stronger growth inhibition. (C) The average-Log GI_{50} values for each KDM5B inhibitor are shown, along with the range representing the difference between the most sensitive and the least sensitive cell lines. (D) Radar charts showing the similarity between each KDM5B inhibitor and the six anticancer drugs that exhibited the highest similarity based on comparison of JFCR39 data. The values represent Pearson's correlation coefficients calculated using the –Log GI_{50} values for each cell line. Correlation analysis was performed by comparing the sensitivity profiles of each JB compound with those of reference anticancer agents included in the JFCR39 database using standard statistical methods implemented in R. The functions of each inhibitor are listed in Table S1.

3.5 | Antitumour Activity of JB-161 in a Subset of NOD/SCID Xenograft Mice

To assess their antitumour efficacy in vivo, we selected JB-157, which showed both a high average activity and broad variability across cell lines, and JB-161, which showed high average activity with low variability, for evaluation in mouse tumor xenograft models. To evaluate the in vivo antitumour effects of JB-157 and JB-161, we used a mouse xenograft model in which human colorectal cancer cells (HT-29) were implanted into NOD/SCID mice. Mice were subsequently assigned to treatment groups receiving DMSO control, 5-fluorouracil (5-FU) alone, JB-157 alone, JB-161 alone, JB-157 combined with 5-FU, or JB-161 combined with 5-FU (Figure 4A). HT-29 cells were selected because they represent a well-characterized and reproducible colorectal cancer xenograft model with detectable KDM5B expression and suitability for downstream transcriptomic and chromatin analyses in vivo. Compared with the control group, JB-157 showed a weak antitumour effect, while JB-161 resulted in pronounced tumor growth inhibition in 3 of 5 mice. 5-FU was selected for the combination experiments because it is a clinically relevant and widely used chemotherapeutic agent in gastrointestinal malignancies. Under the present experimental conditions, combination treatment with 5-FU did not show a clear additional antitumour benefit compared with the corresponding single-agent treatments (Figure 4B). RNA-seq analysis of tumor tissues revealed treatment-associated changes in gene expression following administration of JB-157 or JB-161, compounds with KDM5B inhibitory activity (Figure 4C). Hallmark analysis showed that KRAS SIGNALING UP was enriched upon combination treatment with 5-FU and JB-157, but not with 5-FU and JB-161, compared with the control group (Figure 4D). Compared with the 5-FU group, decreased interferon responses were detected under the combination treatment conditions (Figure 4E). Analysis of cancer stem cell marker gene expression revealed that 5-FU treatment increased CD133 expression, whereas JB-157 or JB-161 did not induce CD133 upregulation (Figure 4F). These findings indicate that treatment with JB-161 was associated with transcriptional alterations in tumor tissues; however, the precise mechanisms underlying its antitumour effects remain to be clarified.

3.6 | JB-161 May, in Some Cases, Reduce the Antitumour Effects of In Vivo CAR-T Cell Therapy

In recent years, the development of in vivo–inducible CAR-T cell therapies has progressed rapidly [27–29]. Inhibition of KDM5B has been reported to enhance tumor cell immunogenicity and promote $CD8^+$ T-cell infiltration and antitumour immunity via activation of the STING pathway and interferon-stimulated genes (ISGs) [30]. Therefore, we hypothesized that JB-161 could serve as a tumor-intrinsic immunogenicity booster to enhance the efficacy of in vivo CAR-T cell therapy. To test this hypothesis, we transplanted the murine colorectal cancer cell line MC38 into C57BL/6 mice and co-administered an LNP-mRNA formulation designed to induce FAP-targeted CAR-T cells (Figure 5A). While treatment with FPC, consisting of 5-FU, anti–PD-1 antibody, and anti–CTLA-4 antibody, failed to completely suppress tumor growth, the addition of mRNA-LNP treatment (FPCR) resulted in near-complete inhibition of tumor progression. Similar antitumour effects were observed in FPCRC, which consisted of FPCR combined with CPI-455 administration, and FPCRJ161, which consisted of FPCR combined with JB-161 administration. However, tumor regrowth was detected in one out of five mice treated with FPCRJ161 (Figure 5B). RNA-seq analysis of excised tumors was performed by comparing the FPCRJ161 group (5-FU, anti–PD-1 antibody, anti–CTLA-4 antibody, mRNA-LNP, and JB-161) with the FPC group (5-FU, anti–PD-1 antibody, and anti–CTLA-4 antibody) and induced marked changes in gene expression, including genes related to apoptosis, neutrophil extracellular trap formation, necroptosis, and the HIF-1 signaling pathway (Figure 5C–E). Gene set enrichment analysis (GSEA) showed that JB-161 treatment was associated with transcriptional changes related to pathways involved in epigenetic regulation, including "PRC2 methylates histones" and "HDAC deacetylates histones" (Figure 5F). Although tumor regrowth was observed in an individual mouse treated with JB-161 combination therapy, further studies with larger cohorts will be required to determine whether JB-161 influences long-term therapeutic responses.

3.7 | JB-157 and JB-161 Induce Chromatin Remodeling

To examine changes in chromatin states induced by KDM5B inhibition, we first performed Western blotting for mono-, di-, and tri-methylated histone H3K4 using HT-29 cells; however, no substantial global changes were observed (Figure 6A and Figure S4). We therefore performed H3 ChIP-seq using the same cell line model to examine genes associated with heterochromatin states, and total H3 ChIP-seq analysis revealed treatment-associated alterations in chromatin occupancy patterns following administration of JB-157 and JB-161 (Figure 6B). Genomic annotation of the detected peak regions showed that,

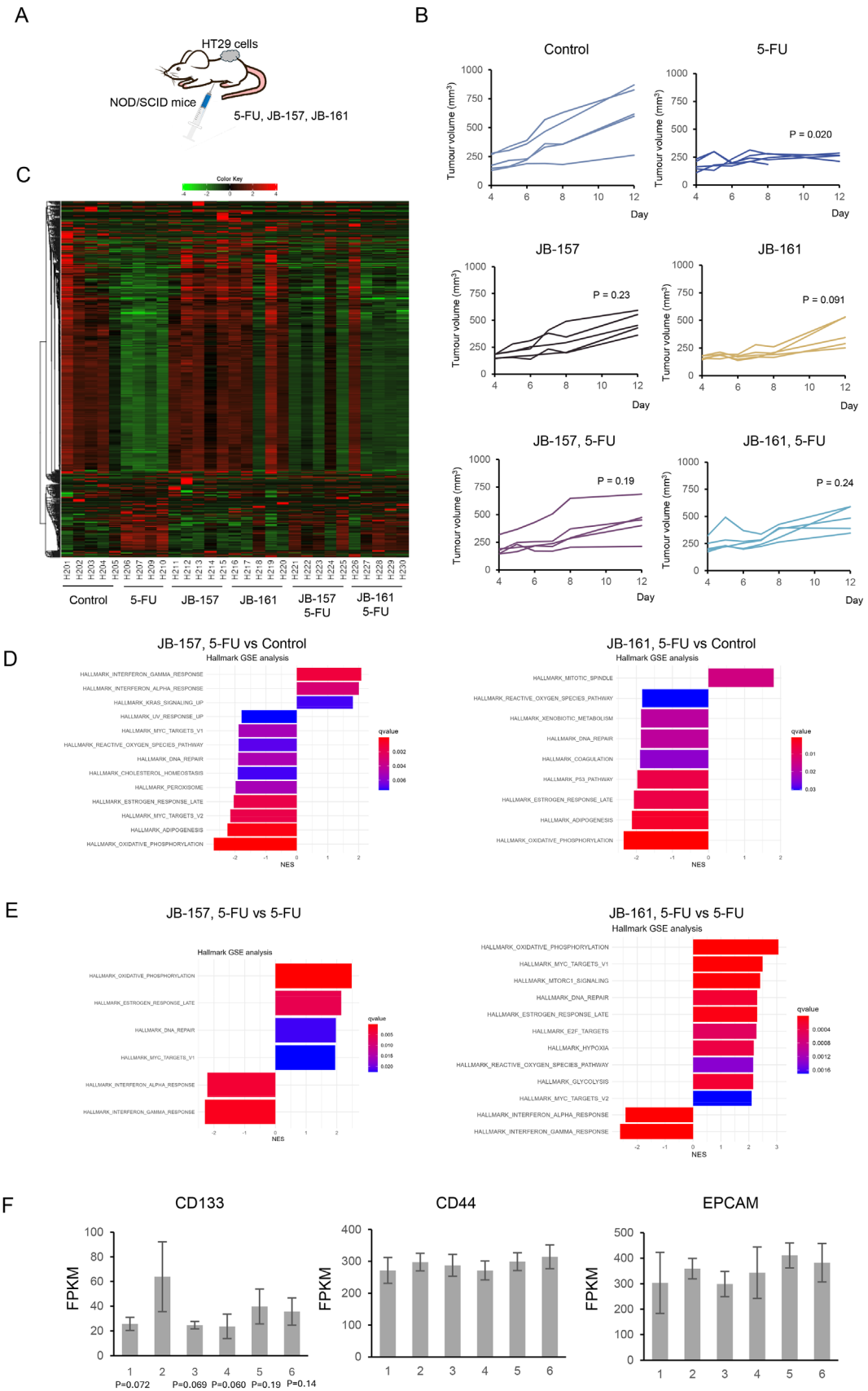

FIGURE 4 | Legend on next page.

FIGURE 4 | JB-161 exhibit antitumour effects in a mouse xenograft model. (A) Schematic overview of the experiment. HT-29 cells were implanted subcutaneously into the backs of NOD/SCID mice. Treatments were administered by intraperitoneal injection on days 4 and 7 after HT-29 cell transplantation. (B) Tumor volume of individual mice was evaluated under six treatment conditions: DMSO (control), 5-FU alone, JB-157 alone, JB-161 alone, JB-157 plus 5-FU, and JB-161 plus 5-FU. The x-axis indicates days after HT-29 cell transplantation. Five mice were used per group. The *p*-values were calculated by unpaired, two-tailed Student's *t*-test compared with the control. (C) Heatmap of the top 2000 differentially expressed genes. Tumors were harvested from mice in each treatment group for RNA sequencing. In the 5-FU–treated group, tumors were collected on day 12 from four mice, excluding one mouse that died on day 8, and RNA was extracted. For all other treatment groups, tumors were similarly collected on day 12, followed by RNA extraction. (D) Hallmark gene set enrichment analysis was performed by comparison with the control group. Hallmark gene sets were detected under the 5-FU combination treatment. Hallmark gene set enrichment analysis was performed by comparison with the control group. NES indicates normalized enrichment score, and q-value indicates the false discovery rate (FDR)-adjusted *p*-value. Pathways with $q < 0.25$ were considered significant. The figure shows representative significantly enriched Hallmark pathways identified in each treatment condition. (E) Hallmark gene set enrichment analysis was performed by comparison with the 5-FU group. Hallmark gene sets were detected under the 5-FU combination treatment. (F) Expression of cancer-related genes. 1 indicates the control; 2, 5-FU; 3, JB-157; 4, JB-161; 5, the combination of JB-157 and 5-FU; and 6, the combination of JB-161 and 5-FU. The *p*-values were calculated by unpaired, two-tailed Student's *t*-test.

compared with control cells, JB-157 treatment was associated with an increased proportion of peaks at promoter regions and a decreased proportion at intronic regions. In contrast, JB-161 treatment resulted in increased peaks at both promoter and intronic regions, accompanied by a reduction in distal intergenic regions (Figure 6C). Treatment with JB-157 and JB-161 was associated with alterations in H3 ChIP-seq peaks at genes involved in cell migration and epithelial homeostasis (Figure 6D). These findings indicate that treatment with JB-157 and JB-161 was associated with chromatin-related alterations; however, the precise contribution of direct KDM5B inhibition to these effects remains to be clarified. To investigate whether JB-161 induces chromatin remodeling during in vivo CAR-T cell therapy, we performed scATAC-seq on tumorus derived from FPCR and FPCRJ161 mice shown in Figure 5. Because tumor growth was markedly suppressed under both conditions, the number of cells available for analysis was limited to 158 cells in the FPCR group and 569 cells in the FPCRJ161 group. UMAP analysis identified two distinct clusters across the conditions (Figure 6E). Compared with FPCR, FPCRJ161 exhibited a strong enrichment of chromatin accessibility at the transcription start site (TSS) of the tumor-suppressive gene *Bax* in cluster 0, whereas cluster 1 showed pronounced accessibility at the TSS of *Il2*, a key regulator of T-cell proliferation (Figure 6F). Analysis of transcription factor activity in immune cells revealed that JB-161 treatment was associated with a reduction in tumor-associated macrophage–like features in macrophage. In dendritic cells, functional antigen-presenting dendritic cells were observed in FPCR, whereas FPCRJ161 exhibited reduced immunogenic features. In addition, activated T cells were detected in FPCR, whereas activated B cells were observed in FPCRJ161 (Figure 6G). Collectively, these findings suggest that JB-161 induces chromatin remodeling not only in cancer cells but also in immune cells. Because tumor growth was markedly suppressed under both conditions, the number of cells available for analysis was limited, particularly in the FPCR group. Therefore, the scATAC-seq findings should be interpreted cautiously and considered exploratory.

4 | Discussion

KDM5B has been reported to be a factor involved in cancer stemness [31]. In triple-negative breast cancer (TNBC), phosphorylation of KDM5B by CDK1 promotes the expansion of stem-like cell populations by enhancing the expression of pluripotency genes such as SOX2 and NANOG [32]. In pancreatic ductal adenocarcinoma (PDAC), KDM5B stabilizes YAP1 via the DLG1 pathway, enhancing cancer stem cells (CSCs) traits and drug resistance [33]. Moreover, KDM5B was shown to maintain hepatocellular carcinoma (HCC) stemness via the YTHDF3/ITGA6 axis [34]. CD133 is a well-known marker of CSCs and CD133 high cancer cells exhibit enhanced tumorigenicity, resistance to radiotherapy, and stem-like transcriptional programs [35]. In the present study, treatment with JB-157 or JB-161 did not induce the upregulation of the CSC-associated marker CD133. These findings may suggest that KDM5B inhibition influences CSC-related transcriptional programs; however, further functional studies will be required to determine whether these compounds directly affect cancer stem cell properties.

We evaluated the growth-inhibitory effects of the final 11 compounds on various cancer cell lines using the JFCR39 panel. The results revealed that each compound exhibited a distinct pattern of growth inhibition. Some compounds showed relatively uniform inhibitory effects across all cell lines, while others displayed variable efficacy depending on the cell type. Notably, the growth-inhibitory effects on HT-29 cells were relatively weak for all compounds compared to the other cell lines. This trend may have also influenced the outcomes observed in the xenograft model using HT-29 cell-transplanted mice. To further demonstrate the efficacy of JB-157 and JB-161, additional in vivo studies using other cancer cell lines will likely be required. In the xenograft model, HT-29 cells were selected because they provide a stable and reproducible colorectal cancer xenograft model and express KDM5B; however, their relatively modest sensitivity to the JB compounds may have influenced the observed in vivo responses. Therefore, further validation using additional tumor models with varying sensitivities to KDM5B inhibition will be necessary to more comprehensively evaluate the therapeutic potential of these compounds.

In hepatocellular carcinoma, knockdown of KDM5B has been reported to increase H3K4 trimethylation at the promoters of cell cycle inhibitory genes such as *p15* and *p27*, leading to reduced cellular proliferation [36]. Consistent with these findings, our study suggests that treatment with JB-157 and JB-161 was associated with alterations in H3 ChIP-seq peak distributions and chromatin-associated signal patterns in cancer cells. However,

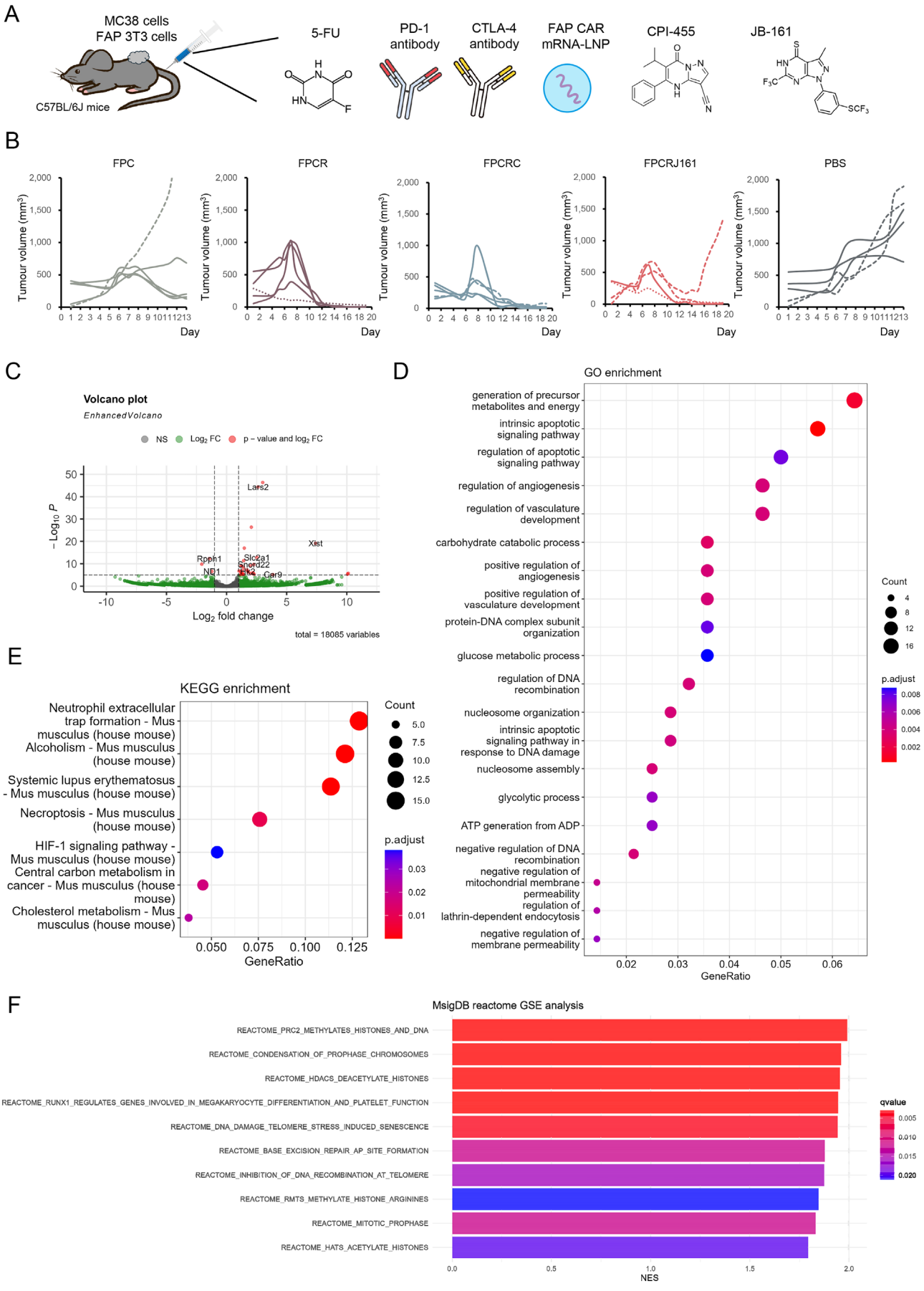

FIGURE 5 | Legend on next page.

FIGURE 5 | JB-161 is compatible with mRNA-LNP that induces FAP-targeting CAR-T cells (A) Schematic overview of the experiment. MC38 and FAP-expressing 3T3 cells were subcutaneously implanted into the dorsal region of C57BL/6J mice, followed by intravenous administration of the compounds. Administration was performed by intravenous injection on days 1, 4, 6, and 8 after tumor implantation. (B) Antitumour efficacy in a mouse xenograft model. PBS group received PBS. FPC group received 5-FU, anti-PD-1, and anti-CTLA-4 antibodies. Other groups received these in combination with: FPCR (mRNA-LNP), FPCRC (mRNA-LNP + CPI455), FPCRJ161 (mRNA-LNP + JB-161). Each line in the graph represents one mouse. The dashed lines in the four conditions other than FPCR indicate mice used for RNA-seq, whereas the dotted lines in the FPCR and FPCRJ161 conditions indicate mice used for scATAC-seq. c–f RNA-seq analysis of gene expression in FPCRJ161 vs. FPC groups. (C) Volcano plot. Differentially expressed genes identified using DESeq2. (D) GO enrichment analysis using clusterProfiler. (E) KEGG enrichment analysis using clusterProfiler. (F) GSEA results.

in the present study, heterochromatin-associated peaks were examined by ChIP-seq, and scATAC-seq analyses were performed on mouse-derived tumor samples. Therefore, further investigation is required to determine which specific promoter regions are directly activated by the JB compounds. Because the present ChIP-seq analysis was performed using a total H3 antibody rather than H3K4 methylation-specific antibodies, the observed changes cannot be directly interpreted as evidence of KDM5B-dependent H3K4 methylation remodeling. Further studies using modification-specific chromatin analyses will be required to clarify the precise epigenetic mechanisms underlying the observed alterations. In addition, KDM5B belongs to the KDM5 family, which includes closely related members such as KDM5A and KDM5C. Whether selective inhibition of KDM5B over other family members can be achieved requires further investigation. Moreover, the precise alterations in cancer stem cell marker gene expression induced by KDM5B inhibition, as well as the underlying mechanisms by which KDM5B regulates their expression, also warrant further study. Furthermore, histone methylation status was not directly evaluated in tumor tissues following in vivo treatment with JB-157 or JB-161. Because KDM5 family members share highly conserved catalytic domains, the selectivity of JB-157 and JB-161 against other KDM5 proteins, including KDM5A and KDM5C, was not comprehensively assessed. Therefore, additional studies using in vivo methylation analyses and broad biochemical specificity profiling will be necessary to fully define the on-target activity and selectivity of these compounds. The effects of JB-161 on immune cell populations and activation states within the tumor microenvironment were not fully evaluated using flow cytometry or functional immunological assays. Therefore, further studies will be required to validate these immunological effects.

This study has several additional limitations. The conclusions regarding immune cell alterations were primarily based on scATAC-seq analyses, which evaluate chromatin accessibility states and transcription factor activity at single-cell resolution, rather than direct quantification of immune cell populations or activation states by flow cytometry. Although scATAC-seq analysis revealed changes in chromatin accessibility patterns and immune cell–associated transcriptional programs, including reduced macrophage-like features, altered dendritic cell characteristics, and differences in lymphocyte-associated signatures following JB-161 treatment, these findings should be interpreted as epigenetic changes suggestive of altered immune cell states rather than definitive evidence of immune cell activation. Therefore, further studies incorporating flow cytometry and functional immunological assays will be necessary to more comprehensively validate the effects of JB-161 on immune cell populations and activation states within the tumor microenvironment. The number of cells available for analysis was limited, particularly in the FPCR group. Therefore, the present scATAC-seq findings should be interpreted with caution and considered exploratory. In addition, further studies using larger cell numbers and independent biological validation will be required to confirm the chromatin accessibility changes suggested by the current dataset. In addition, the current data do not fully clarify whether JB-161 directly induces broad chromatin remodeling programs or which specific genomic loci and cell populations are primarily responsible for these effects. Therefore, additional mechanistic studies will be required to elucidate the direct epigenetic effects of JB-161 in greater detail. HT-29 cells were selected as a reproducible colorectal cancer xenograft model with detectable KDM5B expression; however, because their in vitro sensitivity to JB compounds was moderate compared with several other cell lines, additional validation using alternative tumor models will be important in future studies. Furthermore, histone mark–specific epigenomic analyses, such as H3K4me3- or H3K4me2-specific ChIP-seq, were not performed. Although these approaches would provide greater mechanistic insight into the direct epigenetic consequences of KDM5B inhibition, the present study was primarily designed as a proof-of-concept investigation focused on compound identification and initial biological characterization. Therefore, total H3 ChIP-seq was used to broadly evaluate chromatin-associated changes following treatment with JB compounds. Future studies employing H3K4me3/H3K4me2 ChIP-seq, CUT&RUN, or CUT&Tag analyses will be important for identifying direct promoter-level epigenetic targets and further clarifying the mechanistic relationship between KDM5B inhibition and chromatin remodeling. The scATAC-seq analysis was performed using only one tumor sample per treatment condition. Therefore, the observed chromatin accessibility changes and inferred transcription factor activities should be interpreted as preliminary findings. Additional studies with larger biological cohorts and independent validation experiments will be necessary to confirm the reproducibility and biological significance of these epigenomic alterations. In the NOD/SCID xenograft mouse experiments, under the present experimental conditions, combination treatment with 5-FU did not demonstrate a clear additional antitumour benefit compared with the corresponding single-agent treatments in the HT-29 xenograft model (Figure 4). This may be partly attributable to the relatively modest sensitivity of HT-29 cells to the JB compounds. In addition, the sample size and experimental design may have provided limited statistical power to detect subtle combinatorial effects in vivo. Therefore, further studies using additional colorectal cancer models, optimized dosing regimens, and larger cohorts will be required to more comprehensively evaluate the therapeutic potential and synergistic efficacy of the combination treatment. Substantial

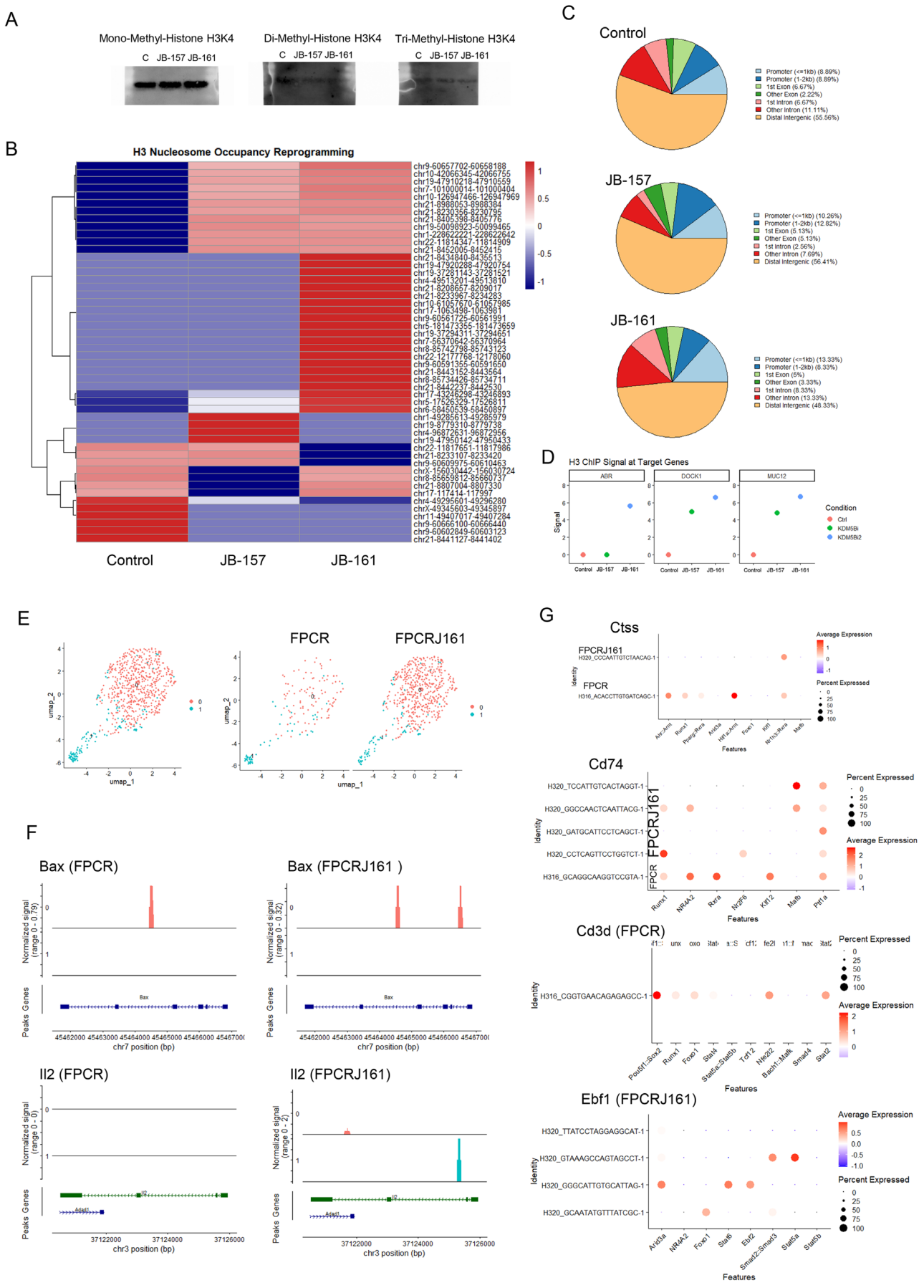

FIGURE 6 | Legend on next page.

FIGURE 6 | KDM5B inhibition induces chromatin remodeling (A) Western blot analysis of mono-, di-, and tri-methylated histone H3K4 following KDM5B inhibition. HT-29 cells were cultured and treated with JB-157 or JB-161 (100 μg), while control cells were treated with DMSO. Uncropped Western blot images are provided in the Supporting Information. Total histone H3 was used as a loading control. (B) Representative ChIP-seq peaks showing marked changes identified using an anti-H3 antibody. (C) Genomic annotation of the detected ChIP-seq peaks. (D) Changes in signal intensity at the ABR, DOCK1, and MUC12 loci under each condition. (E) UMAP projection of individual nuclei detected by scATAC-seq. Tumors derived from FPCR and FPCRJ161 mice indicated by dashed outlines in Figure 5B were analyzed. (F) ChIP-seq and scATAC-seq peaks detected at the Bax and Il2 gene loci. (G) Transcription factor (TF) activity in cells expressing immune cell marker genes. Ctss marks macrophages, Cd74 dendritic cells, Cd3d T cells, and Ebf1 B cells. The y-axis represents barcodes of cells expressing each marker gene, and the x-axis indicates transcription factors associated with immune cell functions.

global H3K4 methylation changes were not observed by Western blotting. Therefore, the current data do not directly establish on-target KDM5B inhibition in cultured cells or tumor tissues. In addition, further mechanistic investigations will be required to determine whether the observed chromatin alterations and antitumour effects are mediated specifically through KDM5B-dependent pathways.

Author Contributions

Masamitsu Konno: conceptualization, investigation, writing – original draft, methodology, validation, visualization, writing – review and editing, software, formal analysis, data curation, resources. **Taroh Satoh:** conceptualization, investigation, funding acquisition, writing – original draft, methodology, validation, visualization, writing – review and editing, software, formal analysis, project administration, data curation, supervision, resources. **Sikun Meng:** conceptualization, investigation, writing – original draft, methodology, validation, visualization, writing – review and editing, software, formal analysis, data curation, resources. **Naohiro Nishida:** conceptualization, investigation, writing – original draft, methodology, validation, visualization, writing – review and editing, software, formal analysis, data curation, resources. **Shingo Dan:** conceptualization, investigation, funding acquisition, writing – original draft, methodology, validation, visualization, writing – review and editing, software, formal analysis, data curation, resources. **Jun Koseki:** conceptualization, investigation, writing – original draft, methodology, validation, visualization, writing – review and editing, data curation, resources, software, formal analysis. **Yasuhiko Kawano:** conceptualization, writing – original draft, investigation, methodology, validation, visualization, writing – review and editing, software, formal analysis, project administration, data curation, resources. **Kanji Meguro:** conceptualization, writing – original draft, methodology, validation, visualization, writing – review and editing, project administration, resources, supervision, data curation, software, formal analysis, investigation. **Shuji Akai:** conceptualization, investigation, funding acquisition, writing – original draft, resources, supervision, data curation, project administration, writing – review and editing. **Nobuhiro Nishiyama:** conceptualization, investigation, writing – original draft, writing – review and editing, visualization, validation, methodology, software, formal analysis, project administration, data curation, supervision, resources. **Hideshi Ishii:** conceptualization, investigation, funding acquisition, writing – original draft, methodology, validation, visualization, writing – review and editing, project administration, formal analysis, software, data curation, supervision, resources. **Masaki Mori:** conceptualization, writing – original draft, writing – review and editing, funding acquisition, validation, resources, project administration, supervision. **Hidetoshi Eguchi:** conceptualization, investigation, funding acquisition, writing – original draft, writing – review and editing, visualization, validation, methodology, software, formal analysis, project administration, data curation, supervision, resources. **Yutaka Miura:** conceptualization, investigation, writing – original draft, resources, supervision, data curation, software, formal analysis, project administration, methodology, validation, visualization, writing – review and editing. **Tomoaki Hara:** conceptualization, investigation, writing – original draft, methodology, validation, visualization, writing – review and editing, software, formal analysis, data curation, resources. **Kazutake Tsujikawa:** conceptualization, resources, project administration, writing – review and editing, visualization. **Toshiya Morie:** conceptualization, investigation, writing – original draft, methodology, validation, visualization, writing – review and editing, software, formal analysis, project administration, data curation, resources.

Acknowledgements

The authors are grateful to all the laboratory members; Drs. A. Asai and K. Kawamoto, the University of Osaka, Japan, for supporting the assessment and analyzed data. The authors thank the Research Institute for Microbial Diseases, the University of Osaka, and the University of Tokyo Center for Frontier Sciences, one of the Integrated Information Analysis Groups of the Platform for Advanced Genome Science, for RNA-seq analysis supports; Molecular Profiling Committee, Grant-in-Aid for Transformative Research Areas "Advanced Animal Model Support (AdAMS)" from The Ministry of Education, Culture, Sports, Science and Technology, Japan (JSPS KAKENHI Grant Number JP 22H04922), for pre-clinical experimental supports. This research was partially supported by Platform Project for Supporting Drug Discovery and Life Science Research (Basis for Supporting Innovative Drug Discovery and Life Science Research (BINDS)) from AMED under Grant Number JP17am0101001, for supports of target compound analysis. This research was partially supported by Research Support Project for Life Science and Drug Discovery (Basis for Supporting Innovative Drug Discovery and Life Science Research (BINDS)) from AMED under Grant Number JP25ama121054, for supports of pharmacological efficacy testing.

Funding

This work was supported by Japan Science and Technology Agency (18KK0251, 19K22658, 20H00541, 21K19526, 22H03146). This work was supported in part by a Grant-in-Aid for Scientific Research from the Ministry of Education, Culture, Sports, Science and Technology (grant nos. 18KK0251, 19K22658, 20H00541, 21K19526, 22H03146, 22K19559, 23K19505, 23K18313, 24K22144, 25K02716, 25K02530, 25H01060, 16H06279 [PAGS], and JP 22H04922). This research was supported by AMED under Grant Number (JP17cm0106414, JP21lm0203007 and JP23ym0126809).

Disclosure

Animal Studies: All experiments in this study were approved by the Osaka University Animal Experiments Committee (Approval No. 30–011-053) and the experiments were conducted in accordance with the Osaka University Regulations on Animal Experiments.

Ethics Statement

Approval of the research protocol by an Institutional Reviewer Board; This study was performed all in mice as mentioned in the animal studies.

Consent

The authors have nothing to report.

Conflicts of Interest

T. H., S. M., and H. I. received partial institutional endowments from Hirotsu Bio Science Inc. (Tokyo, Japan), Kinshu-kai Medical Corporation (Osaka, Japan), Kyowa-kai Medical Corporation (Osaka, Japan), IDEA Consultants Inc. (Tokyo, Japan), Sumitomo Chemical Co. Ltd. (Tokyo, Japan) and Unitech Co. Ltd. (Chiba, Japan). The remaining authors have no competing interests for the present research. No. N. and H. I. is an editorial board member of Cancer Science.

Data Availability Statement

The data that support the findings of this study are available from GEO under the accession number GSE319663, GSE319664 and GSE319665. Restrictions apply to the availability of these data, which were used under license for this study. Data are available from the author(s) with the permission of GEO under the accession number GSE319663, GSE319664 and GSE319665. The scATAC-seq data files have been deposited in Zenodo under the accession number 18653525 (https://zenodo.org/records/18653525).

References

1. B. D. Strahl and C. D. Allis, "The Language of Covalent Histone Modifications," *Nature* 403 (2000): 41–45.

2. T. Kouzarides, "Chromatin Modifications and Their Function," *Cell* 128 (2007): 693–705.

3. M. A. J. Morgan and A. Shilatifard, "Epigenetic Moonlighting: Catalytic-Independent Functions of Histone Modifiers in Regulating Transcription," *Science Advances* 9 (2023): eadg6593.

4. D. E. Handy, R. Castro, and J. Loscalzo, "Epigenetic Modifications: Basic Mechanisms and Role in Cardiovascular Disease," *Circulation* 123 (2011): 2145–2156.

5. J. C. Rice, S. D. Briggs, B. Ueberheide, et al., "Histone Methyltransferases Direct Different Degrees of Methylation to Define Distinct Chromatin Domains," *Molecular Cell* 12 (2003): 1591–1598.

6. Z. H. Gray, M. A. Honer, P. Ghatalia, Y. Shi, and J. R. Whetstine, "20 Years of Histone Lysine Demethylases: From Discovery to the Clinic and Beyond," *Cell* 188 (2025): 1747–1783.

7. K. Agger, P. A. Cloos, L. Rudkjaer, et al., "The H3K27me3 Demethylase JMJD3 Contributes to the Activation of the INK4A-ARF Locus in Response to Oncogene - and Stress-Induced Senescence," *Genes & Development* 23 (2009): 1171–1176.

8. F. Lan, P. E. Bayliss, J. L. Rinn, et al., "A Histone H3 Lysine 27 Demethylase Regulates Animal Posterior Development," *Nature* 449 (2007): 689–694.

9. S. Hong, Y. W. Cho, L. R. Yu, H. Yu, T. D. Veenstra, and K. Ge, "Identification of JmjC Domain-Containing UTX and JMJD3 as Histone H3 Lysine 27 Demethylases," *Proceedings of the National Academy of Sciences of The United States of America* 104 (2007): 18439–18444.

10. J. Yoo, G. W. Kim, Y. H. Jeon, J. Y. Kim, S. W. Lee, and S. H. Kwon, "Drawing a Line Between Histone Demethylase KDM5A and KDM5B: Their Roles in Development and Tumorigenesis," *Experimental & Molecular Medicine* 54 (2022): 2107–2117.

11. L. El Hayek, D. DeVries, A. Gogate, A. Aiken, K. Kaur, and M. H. Chahrour, "Disruption of the Autism Gene and Chromatin Regulator KDM5A Alters Hippocampal Cell Identity," *Science Advances* 9 (2023): eadi0074.

12. E. Brookes, B. Laurent, K. Õunap, et al., "Mutations in the Intellectual Disability Gene KDM5C Reduce Protein Stability and Demethylase Activity," *Human Molecular Genetics* 24 (2015): 2861–2872.

13. B. K. Dey, L. Stalker, A. Schnerch, M. Bhatia, J. Taylor-Papidimitriou, and C. Wynder, "The Histone Demethylase KDM5b/JARID1b Plays a Role in Cell Fate Decisions by Blocking Terminal Differentiation," *Molecular and Cellular Biology* 28 (2008): 5312–5327.

14. B. Xhabija and B. L. Kidder, "KDM5B Is a Master Regulator of the H3K4-Methylome in Stem Cells, Development and Cancer," *Seminars in Cancer Biology* 57 (2019): 79–85.

15. K. Yamane, K. Tateishi, R. J. Klose, et al., "PLU-1 Is an H3K4 Demethylase Involved in Transcriptional Repression and Breast Cancer Cell Proliferation," *Molecular Cell* 25 (2007): 801–812.

16. K. T. Kuo, W. C. Huang, O. A. Bamodu, et al., "Histone Demethylase JARID1B/KDM5B Promotes Aggressiveness of Non-Small Cell Lung Cancer and Serves as a Good Prognostic Predictor," *Clinical Epigenetics* 10 (2018): 107.

17. Z. Yang, J. X. Xu, D. P. Fang, and J. Ke, "Analysis of Key Genes Reveal Lysine Demethylase 5B Promotes Prostate Cancer Progression," *Oncology Letters* 20 (2020): 62.

18. B. R. Leadem, I. Kagiampakis, C. Wilson, et al., "A KDM5 Inhibitor Increases Global H3K4 Trimethylation Occupancy and Enhances the Biological Efficacy of 5-Aza-2'-Deoxycytidine," *Cancer Research* 78 (2018): 1127–1139.

19. G. Paroni, M. Bolis, A. Zanetti, et al., "HER2-Positive Breast-Cancer Cell Lines Are Sensitive to KDM5 Inhibition: Definition of a Gene-Expression Model for the Selection of Sensitive Cases," *Oncogene* 38 (2019): 2675–2689.

20. A. Tumber, A. Nuzzi, E. S. Hookway, et al., "Potent and Selective KDM5 Inhibitor Stops Cellular Demethylation of H3K4me3 at Transcription Start Sites and Proliferation of MM1S Myeloma Cells," *Cell Chemical Biology* 24 (2017): 371–380.

21. V. S. Gehling, S. F. Bellon, J. C. Harmange, et al., "Identification of Potent, Selective KDM5 Inhibitors," *Bioorganic & Medicinal Chemistry Letters* 26 (2016): 4350–4354.

22. W. Dai, X. Qiao, Y. Fang, et al., "Epigenetics-Targeted Drugs: Current Paradigms and Future Challenges," *Signal Transduction and Targeted Therapy* 9 (2024): 332.

23. C. C. Cheng and R. K. Robins, "Potential Purine Antagonists. VI. Synthesis of 1-Alkyl- and 1-Aryl-4-Substituted Pyrazolo[3,4-d]Pyrimidines," *Organic Chemistry* 21 (1956): 1240–1256.

24. J. A. Markwalder, M. R. Arnone, P. A. Benfield, et al., "Synthesis and Biological Evaluation of 1-Aryl-4,5-Dihydro-1H-Pyrazolo[3,4-d] Pyrimidin-4-One Inhibitors of Cyclin-Dependent Kinases," *Journal of Medicinal Chemistry* 47 (2004): 5894–5911.

25. N. Nakatsu, T. Nakamura, K. Yamazaki, et al., "Evaluation of Action Mechanisms of Toxic Chemicals Using JFCR39, a Panel of Human Cancer Cell Lines," *Molecular Pharmacology* 72 (2007): 1171–1180.

26. R. Chijimatsu, S. Kobayashi, Y. Takeda, et al., "Establishment of a Reference Single-Cell RNA Sequencing Dataset for Human Pancreatic Adenocarcinoma," *IScience* 25 (2022): 104659.

27. S. Meng, T. Hara, Y. Miura, et al., "In Vivo Engineered CAR-T Cell Therapy: Lessons Built From COVID-19 mRNA Vaccines," *International Journal of Molecular Sciences* 26 (2025): 3119.

28. S. Meng, T. Hara, T. Sato, et al., "Targeting Fibroblast Activation Protein in Solid Tumors via LNP-Mediated CAR-mRNA Delivery Promotes Durable Regression in Murine Models," *Scientific Reports* 16 (2025): 1624.

29. J. G. Rurik, I. Tombácz, A. Yadegari, et al., "CAR T Cells Produced In Vivo to Treat Cardiac Injury," *Science* 375 (2022): 91–96.

30. S. M. Zhang, W. L. Cai, X. Liu, et al., "KDM5B Promotes Immune Evasion by Recruiting SETDB1 to Silence Retroelements," *Nature* 598 (2021): 682–687.

31. M. Han, W. Xu, P. Cheng, H. Jin, and X. Wang, "Histone Demethylase Lysine Demethylase 5B in Development and Cancer," *Oncotarget* 8 (2017): 8980–8991.

32. I. J. Yeh, E. Esakov, J. D. Lathia, M. Miyagi, O. Reizes, and M. M. Montano, "Phosphorylation of the Histone Demethylase KDM5B and Regulation of the Phenotype of Triple Negative Breast Cancer," *Scientific Reports* 9 (2019): 17663.

33. Y. Wang, S. Liu, B. Li, et al., "KDM5B Promotes SMAD4 Loss-Driven Drug Resistance Through Activating DLG1/YAP to Induce Lipid Accumulation in Pancreatic Ductal Adenocarcinoma," *Cell Death Discovery* 10 (2024): 252.

34. J. C. Guo, Z. Liu, Y. J. Yang, M. Guo, J. Q. Zhang, and J. F. Zheng, "KDM5B Promotes Self-Renewal of Hepatocellular Carcinoma Cells Through the microRNA-448-Mediated YTHDF3/ITGA6 Axis," *Journal of Cellular and Molecular Medicine* 25 (2021): 5949–5962.

35. M. C. Wang, B. F. Wang, H. T. Ren, et al., "Exposure to Endocrine Disruptor DEHP Promotes the Progression and Radiotherapy Resistance of Pancreatic Cancer Cells by Increasing BMI1 Expression and Properties of Cancer Stem Cells," *Ecotoxicology and Environmental Safety* 283 (2024): 116970.

36. D. Wang, S. Han, R. Peng, et al., "Depletion of Histone Demethylase KDM5B Inhibits Cell Proliferation of Hepatocellular Carcinoma by Regulation of Cell Cycle Checkpoint Proteins p15 and p27," *Journal of Experimental & Clinical Cancer Research* 25, no. 35 (2016): 37.

Supporting Information

Additional supporting information can be found online in the Supporting Information section. **Code S1:** Code for scATAC-seq analysis used in Figure 6E–G. **Data S1:** Normalized FPKM values from the RNA-seq data shown in Figure 4. **Data S2:** Normalized read counts from the RNA-seq data shown in Figure 5. **Figure S1:** KDM5B expression and prognosis in cancer tissues. (A) KDM5B expression across cell types in pancreatic cancer scRNA-seq data. Left, feature plot; middle, violin plot; right, UMAP plot annotated with cell types for each cluster. (B) KDM5B expression in cancer cells from pancreatic cancer scRNA-seq data. Left, feature plot; middle, violin plot; right, UMAP plot showing each cluster. (C) Kaplan–Meier analysis of KDM5B expression and prognosis in pancreatic and gastric cancer patients using KM Plotter. **Figure S2:** Synthetic route to compound (I). Compound (I) was synthesized from compound (1) through a six-step process: acid-mediated conversion to compound (2), base-promoted reaction with compound (3) to yield compound (4), thionation, phosphorylation, thiourea coupling, and optional acylation. Key reagents included concentrated sulfuric acid, sodium methoxide, Lawesson's reagent, $POCl_3$, and thiourea. Final purification was done via recrystallization or chromatography. **Figure S3:** Evaluation of JB-157 using the JFCR39 human cancer cell panel. X-axis: $\log_{10}$ drug concentration (M). Y-axis: relative cell growth (%), normalized to untreated controls (100%). Negative values indicate cytotoxic effects. H and L indicate the numbers of compounds showing high and low correlation, respectively, with the fingerprint pattern of the tested compound in the COMPARE analysis based on Log GI_{50} values across the JFCR39 panel. H:0 and L:0 indicate that no compounds with high or low correlation were identified. **Figure S4:** Uncropped Western blot images for Figure 6A. After SDS-PAGE, the PVDF membrane was divided into four sections, and Western blotting was performed using the antibodies indicated in the figure. The images show the membrane sections arranged in order after secondary antibody incubation, and the fluorescence of Alexa Fluor 594 conjugated to the secondary antibodies was detected and imaged. The molecular weights of the marker proteins (kDa), from top to bottom, were 245, 180, 140, 100, 75, 60, 50, 40, 35, 30, 25, 20, 15, and 10. **Table S1:** The functions of each compound shown in Figure 3D. **Table S2:** KDM5B expression levels in each cell line of the JFCR39 panel, as referenced from the Human Protein Atlas.